THE JOURNAL OF PHYSICAL CHEMISTRY A

Subscriber access provided by UNIV OF MICHIGAN

Article

Kinetic Modeling of Methyl Butanoate in Shock Tube

Lam K. Huynh, Kuang C. Lin, and Angela Violi

J. Phys. Chem. A, **2008**, 112 (51), 13470-13480 • DOI: 10.1021/jp804358r • Publication Date (Web): 26 November 2008

Downloaded from http://pubs.acs.org on January 16, 2009

More About This Article

Additional resources and features associated with this article are available within the HTML version:

- Supporting Information
- Access to high resolution figures
- Links to articles and content related to this article
- Copyright permission to reproduce figures and/or text from this article

View the Full Text HTML

ACS Publications
High quality. High impact.

The Journal of Physical Chemistry A is published by the American Chemical Society. 1155 Sixteenth Street N.W., Washington, DC 20036

Kinetic Modeling of Methyl Butanoate in Shock Tube

Lam K. Huynh, Kuang C. Lin, and Angela Violi*

Department of Mechanical Engineering, University of Michigan, Ann Arbor, Michigan 48109-2125

Received: May 16, 2008; Revised Manuscript Received: September 28, 2008

An increased necessity for energy independence and heightened concern about the effects of rising carbon dioxide levels have intensified the search for renewable fuels that could reduce our current consumption of petrol and diesel. One such fuel is biodiesel, which consists of the methyl esters of fatty acids. Methyl butanoate (MB) contains the essential chemical structure of the long-chain fatty acids and a shorter, but similar, alkyl chain. This paper reports on a detailed kinetic mechanism for MB that is assembled using theoretical approaches. Thirteen pathways that include fuel decomposition, isomerization, and propagation steps were computed using ab initio calculations [*J. Org. Chem.* **2008**, *73*, 94]. Rate constants from *first principles* for important reactions in CO_2 formation, namely $CH_3OCO{=}CH_3 + CO_2$ (R1) and $CH_3OCO{=}CH_3O + CO$ (R2) reactions, are computed at high levels of theory and implemented in the mechanism. Using the G3B3 potential energy surface together with the B3LYP/6-31G(d) gradient, Hessian and geometries, the rate constants for reactions R1 and R2 are calculated using the Rice−Ramsperger−Kassel−Marcus theory with corrections from treatments for tunneling, hindered rotation, and variational effects. The calculated rate constants of reaction R1 differ from the data present in the literature by at most 20%, while those of reaction R2 are about a factor of 4 lower than the available values. The new kinetic model derived from ab initio simulations is combined with the kinetic mechanism presented by Fisher et al. [*Proc. Combust. Inst.* **2000**, *28*, 1579] together with the addition of the newly found six-centered unimolecular elimination reaction that yields ethylene and methyl acetate, $MB = C_2H_4 + CH_3COOCH_3$. This latter pathway requires the inclusion of the CH_3COOCH_3 decomposition model suggested by Westbrook et al. [*Proc. Combust. Inst.* **2008**, accepted]. The newly composed kinetic mechanism for MB is used to study the CO_2 formation during the pyrolysis of MB as well as to investigate the autoignition of MB in a shock tube reactor at different temperatures and pressures. The computed results agree very well with experimental data present in the literature. Sensitivity and flux (rate-of-production) analyses are carried out for the CO_2 formation with the new MB mechanism, together with available reaction mechanisms, to assess the importance of various kinetic pathways for each regime. With the new mechanism, the flux analyses for the formation of C_2H species, one of the most important species for ignition delay time, are also presented at different conditions. In addition to giving a better chemical insight of the pyrolysis/oxidation of MB, the results suggest ways to improve the mechanism's capability to predict CO_2 formation and ignition delay times in pyrolysis and oxidation conditions.

1. Introduction

Biodiesel consists of the methyl esters of fatty acids, usually derived from plant oils, although other sources including animal fat are possible. Plant oils are primarily composed of different triacylglycerol molecules with three fatty acid chains (usually 18 or 16 carbons long) esterified to glycerol. The fatty acyl chains are chemically similar to the aliphatic hydrocarbons, which make up the bulk of the molecules found in petrol and diesel. Fatty acid methyl esters (FAMEs) have a formula of $R\text{-}(C{=}O)\text{-}O\text{-}CH_3$ where R is a carbon chain of alkyl or alkenyl with as many as 16−18 carbon atoms.

Biodiesel FAMEs contain two oxygen atoms per molecule. This more oxygenated state compared to conventional diesel leads to lower carbon monoxide production and reduced emission of particulate matter.[1] In addition to containing oxygen, the FAMEs in biodiesel tend to possess one or more double bonds (depending on the triacylglycerol from which they were derived) whereas the hydrocarbons in conventional diesel are completely saturated. These double bonds strongly affect the fuel properties of biodiesel.

Biodiesel are a sustainable source of liquid transportation fuels and they are essentially neutral with respect to the production of carbon dioxide.[2] However, biodiesel fuels introduce new challenges for the development of reaction mechanisms. The long-chain methyl esters, while directly compatible with diesel operation, are generally difficult to study both experimentally and computationally because of their chemical complexity. In terms of kinetic mechanisms, a very large number of reactions is usually needed to model the esters.

Methyl butanoate (MB), $CH_3CH_2CH_2(C{=}O)\text{-}O\text{-}CH_3$ (Figure 1) contains the essential chemical structure of the long-chain fatty acids, i.e., the methyl ester termination and a shorter, but similar, alkyl chain.[3−8] In addition, detailed reaction mechanisms for MB are of a manageable size. Due to the large size of existing kinetic models for MB (usually in the order of thousands of reactions), rate constants of a significant number of elementary reactions are usually estimated from reactions available in the literature.[3−5,7,8]

Our group has recently reported a study on potential pathways for MB breakdown using ab initio calculations. In this follow-up paper, we extend this study to develop a kinetic mechanism for MB based on reaction pathways and rates identified using

* Corresponding author. E-mail: avioli@umich.edu.

10.1021/jp804358r CCC: $40.75 © 2008 American Chemical Society
Published on Web 11/26/2008

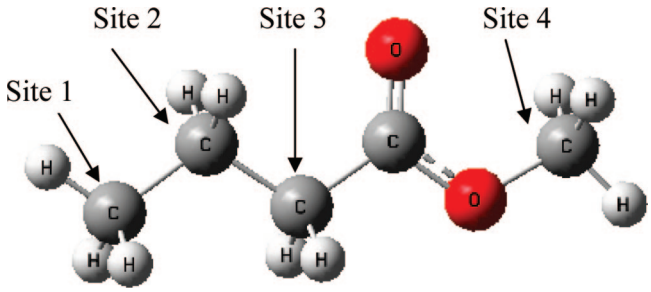


Figure 1. Structure of methyl butanoate.

TABLE 1: Barrier Heights for Hydrogen Abstraction Reactions at Different Sites of MB by Different Radicals[a]

	site 1 (MB4J)	site 2 (MB3J)	site 3 (MB2J)	site 4 (MBMJ)
MB + H	8.3	6.5	6.0	8.4
MB + OH	5.0	1.9	4.1	6.2
MB + CH_3	17.0	15.2	13.5	16.2

[a] The numbers (kcal/mol) are obtained at the BH&HLYP/cc-pVTZ level of theory.

quantum chemistry and dynamics calculations.[6] One of the main goals of this work is to obtain a kinetic mechanism to predict the formation of CO_2 in pyrolitic conditions such as shock tube experiments. Rate constants for important reactions in CO_2 formation/consumption, namely $CH_3OCO{=}CH_3 + CO_2$ (R1) and $CH_3OCO{=}CH_3O + CO$ (R2) reactions, are computed using high levels of quantum mechanics and direct dynamics. The ab initio submodel is then combined with the kinetic mechanism presented by Fisher et al.[3] together with the addition of the newly found six-centered unimolecular elimination reaction that yields ethylene and methyl acetate (CH_3COOCH_3),[5,9] and the methyl acetate decomposition model.[10] The newly composed kinetic model is then used to simulate the formation of carbon dioxide[11] and ignition delay time[8] in shock tube experiments using MB as fuel.

2. Kinetic Model

Our group has recently reported results on reaction pathways for the breakdown of MB using quantum mechanics calculations.[6] Electronic structures and structure-related molecular properties of reactants, intermediates, products (e.g., CO and CO_2), and transition states were explored at the BH&HLYP/cc-pVTZ level of theory. These results are used as initial data to develop a MB mechanism that can predict CO_2 in pyrolysis conditions as well as autoignition characteristics of the fuel.

2.1. Fuel Decomposition Steps. Rate constants for reactions involving hydrogen abstraction from MB by reactive flame radicals such as H, OH, and CH_3 were calculated using the transition state theory (TST) and the BH&HLYP/cc-pVTZ level of theory. These bimolecular reactions show very low barrier heights when compared with unimolecular reactions, either simple (one bond breaking at a time) or complex (multiple bonds breaking and forming at the same time) fission. For example, H abstraction from MB by H atoms has an average reaction barrier at different sites (with the zero-point energy correction) of ~7 kcal/mol at the BH&HLYP/cc-pVTZ level[6] while the lowest barrier for the unimolecular decomposition is about 70 kcal/mol.[9]

The barrier heights for hydrogen abstraction reactions at a specific site depend on the type of attacking radicals. Table 1 reports the comparison between the energy barriers for the reactions of MB with H, OH, and CH_3 to form four MB radicals,

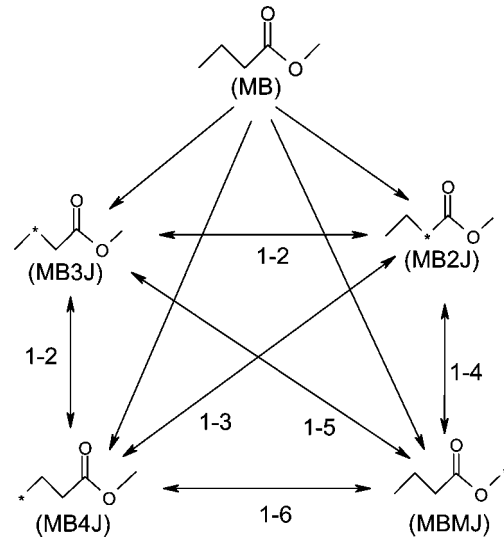


Figure 2. Isomerization reactions between initial MB radicals (MBMJ, MB2J, MB3J, and MB4J). "1−x" denotes the 1−x hydrogen migration reaction. Abbreviations used by Fisher et al.[4] for MB radicals are given in parentheses.

TABLE 2: Barrier Heights for the Isomerization Reactions at the BH&HLYP/cc-pVTZ Level of Theory

type of migration reaction	reaction	barrier height (kcal/mol)
1−2	MB4J → MB3J	35.4
1−3	MB4J → MB2J	32.6
1−6	MB4J → MBMJ	22.5

MB3J, MB2J, MB4J, and MBMJ. The sketchy structures of these radicals are reported in Figure 2. The barrier heights for hydrogen abstraction reactions with OH and H (about 4.3 and 7.3 kcal/mol at the BH&HLYP/cc-pVTZ level of theory, respectively) are considerably lower than those for reactions by the CH_3 radicals (the averaged value of 15.5 kcal/mol). In addition, for the same reacting radical, the barrier height values depend on the site of the abstraction but the difference is not significant. The reactions at the terminal carbons (-CH_3 group) have higher barriers (3 kcal/mol) than those at nonterminal carbon (-CH_2- group).

2.2. Isomerization Steps. The four initial MB radicals (cf. Figure 2) can undergo hydrogen isomerization. These reactions are responsible for the distribution of MB radicals that are important in the propagation steps through β-scission reactions. The energy barriers depend on the type of hydrogen migration, namely 1−2, 1−3, 1−4, 1−5 and/or 1−6 hydrogen migration reactions (see Figure 2). If the reaction proceeds through a transition state having a low ring constraint energy (e.g., seven-membered ring for the 1−6 hydrogen migration reaction), the barrier height is lower than that of a transition state involving a four-membered ring (e.g., 1−3 hydrogen migration). Table 2 shows the barrier heights for three of the isomerization reactions depicted in Figure 2, obtained at the BH&HLYP/cc-pVTZ level of theory.

2.3. Propagation Steps. Besides isomerization, the four initial MB radicals can undergo β-scission reactions. In our previous publication, we identified 13 pathways for the breakdown of MB leading to the formation of small molecules such as CO, H_2CO, CH_3, C_2H_3, and C_2H_4.[6] The rates for 26 reactions (forward and reverse) are computed using the Rice−Ramsperger−Kassel−Marcus (RRKM) and TST theories with the corrections for hindered rotation and tunneling treatments.

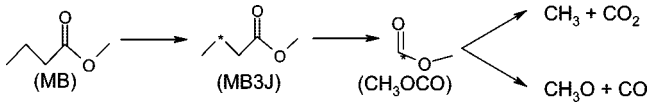


Figure 3. Main reaction pathways for CO_2/CO formation.

A detailed analysis of the reaction pathways identified important pathways for the formation of CO and CO_2. Specifically, radical $CH_3CHCH_2C(O)OCH_3$ (MB3J), which is formed by H abstraction reaction with an energy barrier of 6.5 kcal/mol, decomposes through a β-scission reaction to form C_3H_6 (propylene) and CH_3OCO. The pathway is reported in Figure 3. Methoxylcarbonyl radical, CH_3OCO, is known to be an important intermediate of the reaction of carbon monoxide (CO) with the methoxyl radical (CH_3O).[12] Intermediate CH_3OCO can form $CH_3O + CO$ and $CH_3 + CO_2$ breaking C−O bonds. The second product channel ($CH_3 + CO_2$) has a lower barrier of 16.6 kcal/mol as compared to 20.8 kcal/mol to produce $CH_3O + CO$.

The MB3J radical plays a significant role in the combustion of oxygenated compounds such as alcohol, ether, and ester. Particularly, it has been identified as the main intermediate directly producing CO and CO_2 in the combustion of dimethyl carbonate ($(CH_3O)_2CO$) in opposed-flow diffusion flames[13] and in shock tube simulations.[11] It is, therefore, crucial to have accurate rate constants for the two following reactions, in order to be able to reproduce the CO_2 concentration profiles correctly.

$$CH_3OCO = CH_3 + CO_2 \quad \text{(R1)}$$

$$CH_3OCO = CH_3O + CO \quad \text{(R2)}$$

Reaction R1 is mainly responsible for CO_2 formation while reaction R2 is the main competing reaction in consuming CH_3OCO; thus, it is also important in CO_2 production. The importance of reaction R2 in CO_2 formation is discussed in the section of the sensitivity analysis and rate-of-production analysis.

The rate constants for reaction $CH_3 + CO_2 = CH_3OCO$ (R-1) and $CH_3O + CO = CH_3OCO$ (R-2) were first estimated by Fisher et al.[3] based on similarity. In 2005, Glaude et al.[13] used the transition state theory to calculate the rate constants with the potential energy surface computed at CBS-Q methods. In the study, quantum effects, namely tunneling and recrossing effects, were not included in the calculated rate constants. The rate constants for R1 and R2 were then obtained using thermodynamic properties of the species and TST rate constants of reactions R-1 and R-2, respectively. Using quantum mechanics calculations, McCunn et al.[12] studied the potential energy surface of this reaction, but they did not report explicit values for the rate constants in their study.

Below, we employ high levels of quantum mechanics and direct dynamics methods to study reactions R1 and R2. The new rate constants were included in the MB mechanism to improve the prediction of CO_2 concentration profiles[11] and autoignition measurements in shock tube. The updated mechanism was also used to model autoignition data of MB.

3. Computational Details

All of the electronic structure calculations were carried out using the Gaussian 03 program.[14] The G3-method variant (denoted as G3B3)[15] using geometries and zero-point energies obtained from B3LYP density functional theory [B3LYP/6-31G(d)] was used to obtain accurate energetic data for these reactions. The variant is believed to give the energetic information within the chemical accuracy, e.g., 1 kcal/mol. The minimum energy path (MEP) connecting reactant(s) and product(s) is also obtained at the B3LYP/6-31G(d) level using the intrinsic reaction path (IRC) method. The IRC calculation traces the steepest descent path from the transition state to the corresponding reactant(s) and product(s) using the Gonzalez−Schlegel method[16] with a step size of 0.2 $(amu)^{1/2}$ bohr for a total of 200 steps. The gradient and Hessian for 30 selected points (15 points in each reactant and product channels) along the MEP were obtained at the B3LYP/6-31G(d) level. The selected points along the MEP were chosen using the autofocusing technique,[17] which uses a combination of the barrier shape, and the second derivatives of the Z-matrix geometrical parameters (along the MEP) to predict the regions along the MEP that are sensitive in rate determination.

The rate constants were calculated employing the kinetic module of the web-based computational science and engineering online (CSE-Online) environment.[18] The RRKM theory[19,20] together with the one-dimentional Eckart methodology[21,22] is used to calculated rate constants for reactions R1 and R2. Rate constants for the reverse reactions, namely reactions R-1 and R-2, are obtained from those of R1 and R2 and thermodynamic properties of the species (reactant(s) and product(s)). For reaction R2, due to the flat potential energy surface (cf. Figure 6), variational effect is included in the rate constant calculation. A more accurate tunneling correction method such as small curvature tunneling (SCT) correction[23−25] was also obtained in order to confirm the Eckart tunneling values. Hindered rotation corrections of CH_3 group along the C−O bond (in both CH_3OCO and CH_3—OCO transition state to form CH_3 and CO_2) and CO group along C−O bond (in CH_3O—CO transition state to form CH_3O and CO) are also incorporated in the calculated rate constants using the approach proposed by Ayala and Schlegel.[26] This formalism optimizes the accuracy for treating a single rotor to minimize the compound errors in the case of multiple internal rotors. In order to calculate the hindered rotation correction factor for a certain vibrational mode to the partition function, the vibrational mode, the rotating group, as well as the periodicity number of the torsional potential must be identified. From the given information together with the geometry of the interested molecule, information needed for calculating the correction factor of hindered rotation treatment, e.g., reduced moment of inertia and the periodic potential, can be obtained. The correction factor is then calculated using a fitting formula [ref 26 - eq 26] which was derived from the tabulated accurate values to improve upon Pitzer and Gwinn's formula.[27,28] The fitting formula retains the positive characteristics of Pitzer and Gwinn's formula for high V_0/kT while improving its behavior for low V_0/kT, where V_0 is the internal rotation barrier height.

Discretely calculated values of rate constants for a reaction at different temperatures were fitted to the modified Arrhenius expression as $k(T) = A \times T^n \times \exp(-E_a/RT)$ in the temperature range of 300−2500 K.

4. Results and Discussion

4.1. Rate Constant Calculation. Figure 4 shows the potential energy surface of the decomposition of CH_3OCO to form $CH_3 + CO_2$ and $CH_3O + CO$ at different levels of theory. CH_3OCO radical has two conformations (*cis* and *trans*) whose energies are very similar with the difference of about 0.3 kcal/mol at G3B3 level. The *trans* conformation can only produce $CH_3O + CO$ with the barrier of 21.5 kcal/mol, while it can decompose to form $CH_3 + CO_2$ with the barrier of ~33 kcal/mol[12] which is much higher than that from the *cis* configuration

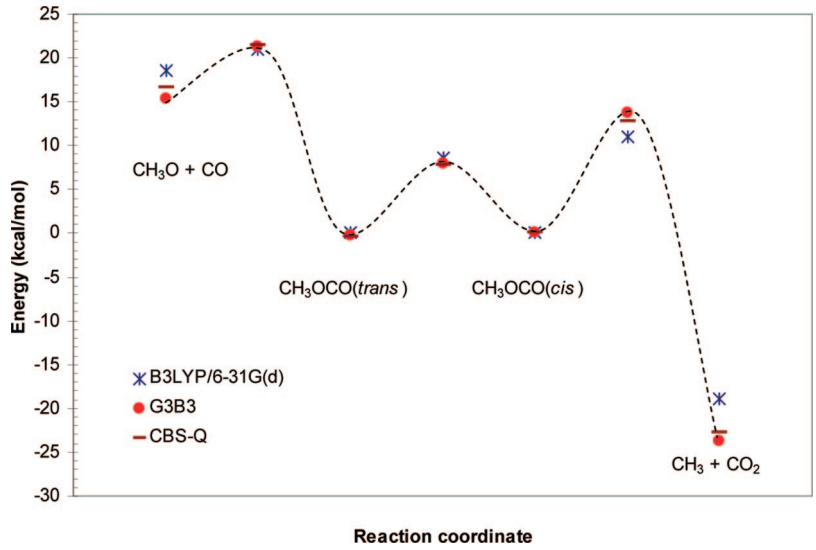


Figure 4. Potential energy surface of the decomposition of CH_3OCO radical. All energy is relative to the energy of the *cis* conformation of CH_3OCO radical, denoted as $CH_3OCO(cis)$.

(~14 kcal/mol). For this reason, in this study we only consider the *cis* conformation is considered for the $CH_3 + CO_2$ channel. Figure 5 shows the geometric parameters for the two conformations of CH_3OCO radical (*cis* and *trans*) as well as the transition state for two decomposition channels at the B3LYP/6-31G(d) level.

It is observed that the barrier height for the isomerization from *cis* to *trans* conformation is significantly lower than those of decomposition channels (7.9 kcal/mol compared to 13.7 and 21.5 kcal/mol for CO_2 and CO channels at G3B3 level, respectively), and the thermodynamic properties ($\Delta H^{\circ}_{f,298K}$, S, C_p) of these two conformations are very similar. Therefore, only one species name, namely CH_3OCO, is used to represent both conformations in order to simplify the mechanism. This assumption is valid since the inclusion of this isomerization pathway in our mechanism does not affect the results presented in this study.

The potential energy surface for the decomposition of CH_3OCO radical has been calculated by Good and Francisco,[29] using the G2 level of theory. The authors recommended the values of 14.7 and 21.8 kcal/mol for the barrier height ($\Delta V^{\ddagger}$) for reaction R1 and R2, respectively. In 2005, Glaude et al.[13] used the CBS-Q method to calculate the rate constants and thermodynamic data for related species, reporting barrier heights of 14.7 and 22.7 kcal/mol to CO_2 and CO, respectively. Most recently, using G3B3 level of theory, McCunn et al.[12] computed the value of 13.8 and 21.6 kcal/mol for the barrier height for reaction R1 and R2, respectively. Table 3 lists energetic data for the two reactions R1 and R2.

The latest versions of composite methods such as the G3 method by Curtis et al.[15] and CBS-QB3 method by Peterson and co-workers[30] can achieve average accuracies of about 1 kcal/mol when compared to a large set of well-established experimental values; while the early G2 and CBS-Q methods are known to give an accuracy of about 2 kcal/mol. Therefore, the electronic structure calculation results obtained from G3B3, a G3-method variant, are more reliable than those from both G2 and CBS-Q.

In this study, the G3B3 level of theory was used to obtain accurate energetic data for reactions R1 and R2. The B3LYP/6-31G(d) MEP was scaled to obtain the G3B3 vibrationally adiabatic ground-state potential curve $V^{g}_{a}(s)$, where s is the reaction coordinate. The reaction coordinate s is defined as the distance along the MEP with the origin located at the saddle point, and it is positive on the product side and negative on the reactant side. The $V^{g}_{a}(s)$ is the sum of the classical adiabatic ground-state potential curve $V_c(s)$ and the vibrational zero-point energy (VZPE) which was calculated using the B3LYP Hessian data (frequencies) with the scaling factor of 0.96. Figure 6 shows the minimum energy path $V^{g}_{a}(s)$ for reactions R1 and R2 in the vicinity of the transition states.

4.1.1. Rate Constants for $CH_3OCO \rightarrow CH_3 + CO_2$ (R1). Using the G3B3 potential energy surface together with the B3LYP/6-31G(d) gradient, Hessian and geometries, rate constants for the title reaction are computed using different methods with the corrections from tunneling and hindered rotation treatments. Eckart tunneling was included in the RRKM calculation,[21] while SCT was taken into account for other methods such as canonical variational transition state theory (CVT) and microcanonical variational transition state theory (MVT).[31,32] The rotation of the CH_3 group along the $C(H_3)$—O(CO) axis at the reactant and the transition state (cf. Figure 5) was treated as a hindered rotor.

Figure 7 shows the computed rate constants at different temperatures. Since the tunneling factor is close to unity, the tunneling effect is not important for this reaction and decreases with the temperature. For example, the SCT treatment increases the total rate by a factor of 2.2 and 1.08 at 300 and 1000 K, respectively. On the contrary, the correction factor for the hindered rotation (HR) treatment decreases the rate constants noticeably, and the HR effect increases with the temperature. The HR treatment lowers the total rate by a factor of 0.44 and 0.34 at 300 and 1000 K, respectively. It is interesting to find that the three methods, RRKM/Eckart/HR, CVT/SCT/HR, and MVT/SCT/HR, give very similar results in the whole temperature range 300−2500 K (cf. Figure 7). Particularly, the CVT/SCT/HR method gives the middle results between the RRKM/Eckart/HR and MVT/SCT/HR with the maximum difference of 50% in the whole temperature range. The modified Arrhenius expression for the rate constants calculated at the RRKM/Eckart/HR in the temperature range of 300−2500 K is

$$K_{R1}(T) = 1.55 \times 10^{12} \times T^{0.514} \times \exp(-15173/RT), \quad (\text{unit: s}^{-1}) \quad (1)$$

Our calculated rate constants are similar to those proposed by Glaude et al.,[13] within a difference of 20% for the whole temperature range. Particularly, the new rate constants are 18% higher and 14% lower than Glaude's data at 300 and 1500 K, respectively.

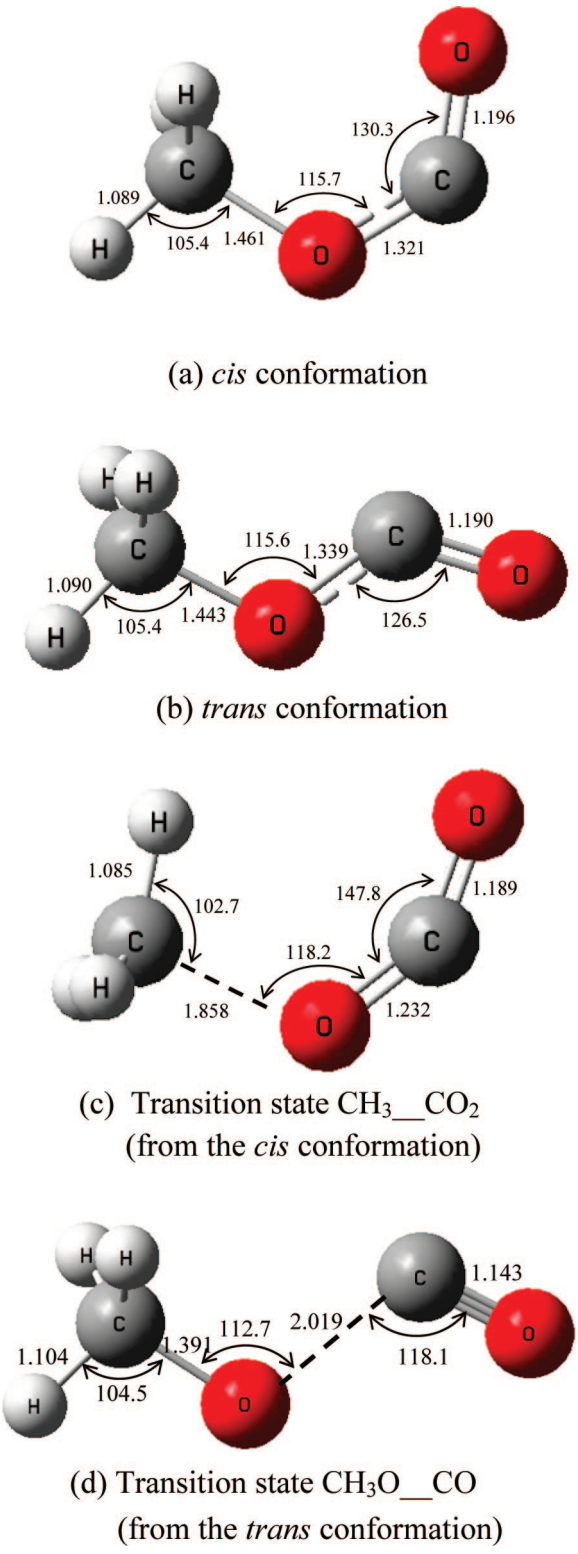


Figure 5. Optimized geometries for CH_3OCO radial (a) *cis* conformation, (b) *trans* conformations, (c) transition state to $CH_3 + CO_2$, and (d) transition state to $CH_3O + CO$. Bond lengths are in angstroms, and angles are in degrees.

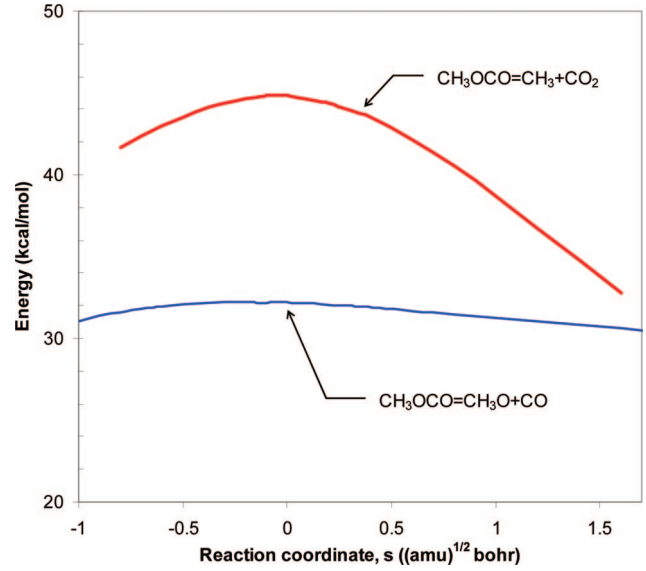


Figure 6. G3B3 minimum energy path in the vicinity of the transition state ($s = 0$) for two channels: $CH_3OCO = CH_3 + CO_2$ (R1) and $CH_3OCO = CH_3O + CO$ (R2). The energy $V_a^e(s)$ is relative to the classical energy (no zero-point energy correction included) of the reactant, CH_3OCO. CH_3OCO is at $s = -\infty$, while decomposition products ($CH_3 + CO_2$ and $CH_3O + CO$ for R1 and R2, respectively) are at $s = +\infty$.

TABLE 3: Energetic Information for the Reaction $CH_3OCO = CH_3 + CO_2$ (R1) and $CH_3OCO = CH_3O + CO$ (R2) at Different Levels of Theory[a]

level of theory	$\Delta V^{\ddagger}$	ΔE	$\Delta V^{\ddagger}_{\text{reverse}}$	ref
	$CH_3OCO = CH_3 + CO_2$ (R1)			
G2	14.7	−21.6	36.3	29
CBS-Q	12.8 (14.7[b])	−22.77	35.52	this study
G3B3	13.7	−23.7	37.43	this study (also ref 12)
	$CH_3OCO = CH_3O + CO$ (R2)			
G2	21.8	15.2	6.6	29
CBS-Q	21.8 (22.7[b])	17.0	4.8	this study
G3B3	21.5	15.6	5.9	this study (also ref 12)

[a] Values are in kcal/mol. [b] The values in parenthesis are from Glaude et al.[13] using the CBS-Q method.

4.1.2. Rate Constants for $CH_3OCO \rightarrow CH_3O + CO$ (R2). Similarly, rate constants for reaction R2 are derived using the G3B3 potential energy surface together with the B3LYP/6-31G(d) gradient, Hessian and geometries. Because the minimum energy path for the $CH_3OCO = CH_3O + CO$ channel in the transition state vicinity is rather "flat" (cf. Figure 6), inclusion of variational effect is expected to give more accurate rate constants for this reaction. Rate constants for this channel were derived using RRKM method with the variational treatment. Corrections from Eckart tunneling and hindered rotation treatments were also included. In addition to the rotation of the CH_3 group along the C(H$_3$)—O(CO) axis at the reactant and the transition state, the rotation of CO group along the CH$_3$O—CO axis in the transition state (cf. Figure 5d) is also considered as a hindered rotor.

Similar to reaction R1, the contribution from tunneling treatment is small for the wide temperature range; specifically the tunneling factor is close to unity. While the HR treatment lowers the rate constants of reaction R1, it increases rate

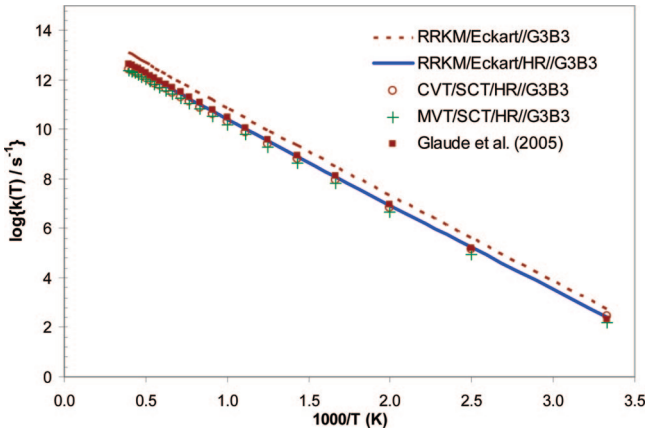


Figure 7. Arrhenius plot of the calculated rate constants and available data from the literature for the $CH_3OCO = CH_3 + CO_2$ reaction.

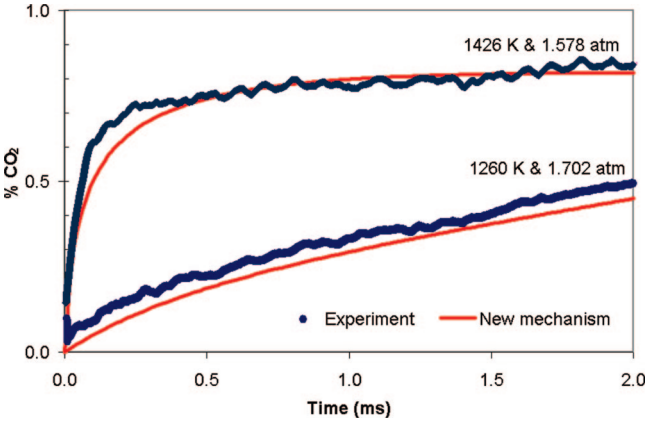


Figure 8. Mole fraction profiles of CO_2 for MB pyrolysis (2% MB in Ar) as a function of time at reflected shock conditions: (a) $T = 1260$ K and $P = 1.702$ atm and (b) $T = 1426$ K and $P = 1.578$ atm.

TABLE 4: Main Reactions for the Formation of CO_2 during MB Pyrolysis[a]

reactions	no.
$CH_3OCO = CH_3 + CO_2$	(R1)
$CH_3OCO = CH_3O + CO$	(R2)
$CH_3CH_2CH_2COO$ (BAOJ) + CH_3 = MB	(R3)
MB + H = $CH_3CHCH_2COOCH_3$ (MB3J) + H_2	(R4)
$CH_3CHCH_2COOCH_3$ (MB3J) = $CH_3OCO + C_3H_6$	(R5)
MB + H = $CH_2CH_2CH_2COOCH_3$ (MB4J) + H_2	(R6)
$CH_2CO_2CH_3 + C_2H_5$ = MB	(R7)
$CH_3CH_2CH_2COO$ (BAOJ) = n-$C_3H_7 + CO_2$	(R8)
MB = n-$C_3H_7 + CH_3OCO$	(R9)
MB = $CH_3 + CH_2CH_2COOCH_3$ (MP3J)	(R10)
$CH_2CH_2COOCH_3$ (MP3J) = $C_2H_4 + CH_3OCO$	(R11)
MB + H = $CH_3CH_2CH_2COOCH_2$ (MBMJ) + H_2	(R12)
$CH_3CH_2CH_2COOCH_2$ (MBMJ) = $CH_3CHCH_2COOCH_3$ (MB3J)	(R13)

[a] Abbreviations used by Fisher et al.[4] for selected MB-related radical species are given in parentheses.

constants of reaction R2 with temperature. For example, the rate constants are 2.4 and 2.7 times faster at 1000 and 1500 K, respectively. This rate constant increase can be explained by the HR treatment of the rotation of CO group along the CH_3O—CO axis in the transition state which is not treated as a hindered rotor in reaction R1. The variational effect is found to be more important for this reaction than for reaction R1 due to the "flat" potential energy surface. For example, the variational treatment lowers the rate by a factor of 2.4 and 2.1 at 1000 and 1500 K, respectively. The modified Arrhenius expression for

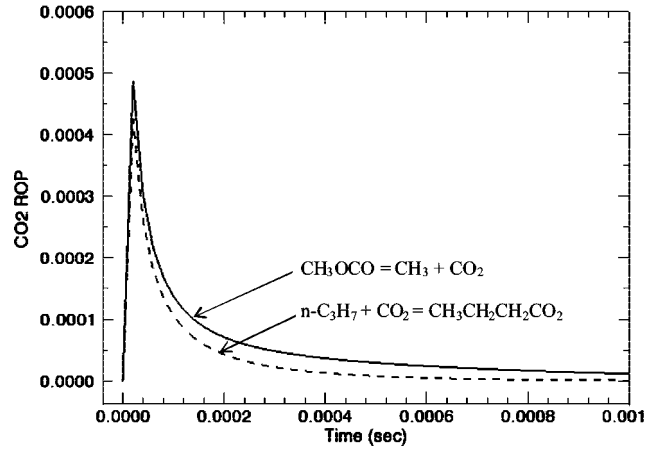


Figure 9. Rate-of-production (ROP) for CO_2 as a function of time at initial conditions of 1426 K, 1.58 atm, and 2% MB in argon for the two most important reactions in the CO_2 formation.

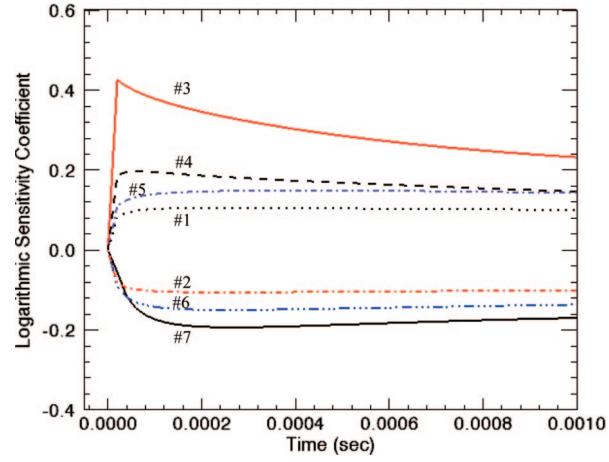


Figure 10. Sensitivity analysis for CO_2 as a function of time at initial conditions of 1426 K, 1.58 atm, 2% MB in argon. The seven largest sensitivity coefficients are shown.

the rate constants calculated in the temperature range of 300−2500 K is

$$K_{R2}(T) = 7.37 \times 10^{12} \times T^{0.479} \times \exp(-23792/RT), \quad (\text{unit: s}^{-1}) \quad (2)$$

By effectively varying the dividing surface along the MEP between the reactants and products, variational treatment minimizes the recrossing effects, lowering the calculated rate constant, e.g., TST rate constant. Our rate constants for reaction R2 are found 4 times lower than those introduced by Glaude et al. at 1500 K. Considering the smaller difference in the rate constants for R1 compared with R2, the difference in the latter is responsible for the higher CO_2/CO branching ratio compared to that proposed by Glaude et al.

4.1.3. Rate Constants for $CH_3 + CO_2 \rightarrow CH_3OCO$ (R-1) and $CH_3O + CO \rightarrow CH_3OCO$ (R-2). With the use of thermodynamic properties of related species calculated at G3B3 level of theory and the calculated rate constants for reactions R1 and R2, rate constants for reverse reactions R-1 and R-2 can be accurately derived, respectively. The rate constants for reaction R-1 and R-2 can be expressed using the modified Arrhenius form as

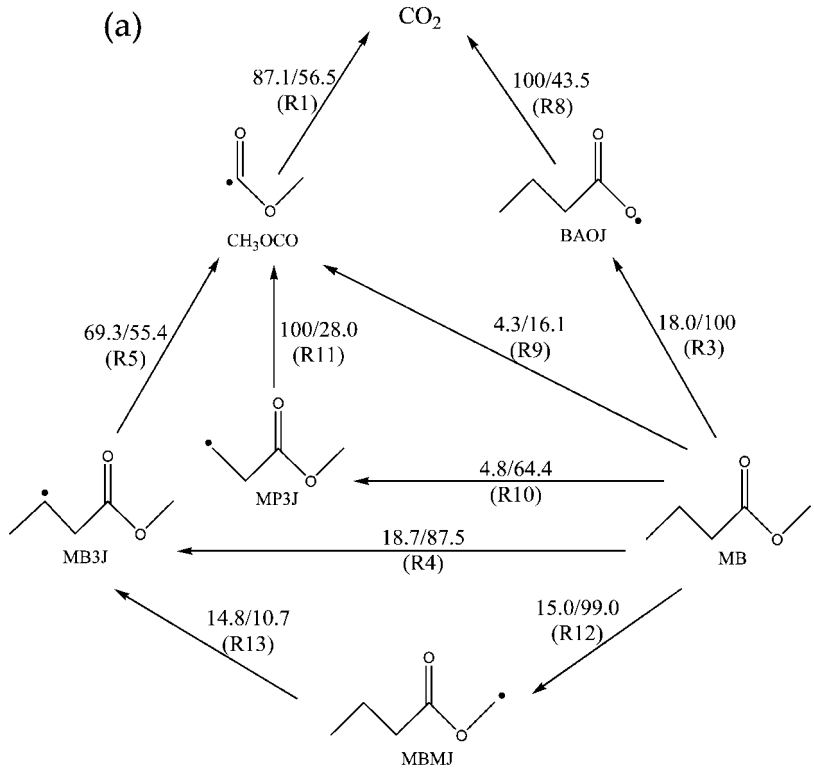
$$k_{R-1}(T) = 6.89 \times 10^{6} T^{1.774} \exp(-18459/RT), \quad (\text{unit: cm}^3\ \text{mol}^{-1}\ \text{s}^{-1}) \quad (3)$$

$$k_{R\text{-}2}(T) = 7.10 \times 10^5 T^{1.897} \exp(-3356/RT),$$

(unit: $cm^3\ mol^{-1}\ s^{-1}$) (4)

4.2. New Kinetic Mechanism for Methyl Butanoate. The new pathways and reaction rates for MB decomposition were embedded into the latest version of the chemical model presented by Fisher et al.[3] (version 2004 obtained at http://www-cmls.llnl.gov/ composed of 264 species and 1219 reactions.

In addition to the simple unimolecular decomposition (one bond breaking at a time), the six-centered unimolecular elimination reaction (multiple bonds breaking and forming at the same time) yielding ethylene and methyl acetate[5,9] was included in



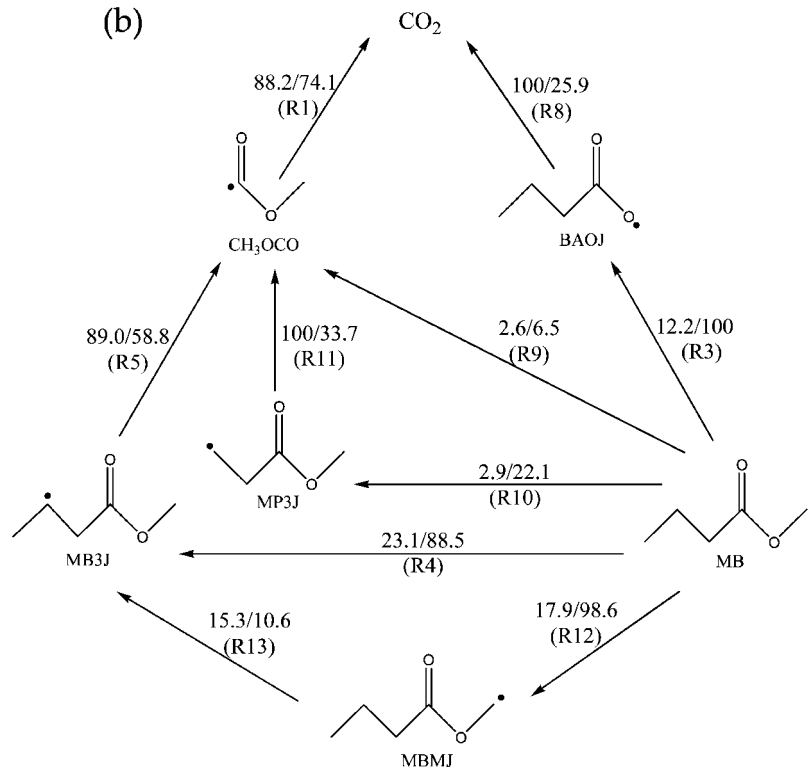


Figure 11. Flux analyses for the formation of CO_2 during the MB pyrolysis at $T = 1426$ K and $P = 1.578$ atm in the shock tube. The analysis was carried out with the new kinetic mechanism at different residence times: (a) $\tau = 0.1$ ms and (b) $\tau = 0.4$ ms. The most important reactions involved in each pathway are given in parentheses. The notation "A/B" means A% reactant produces B% product in the considered channel.

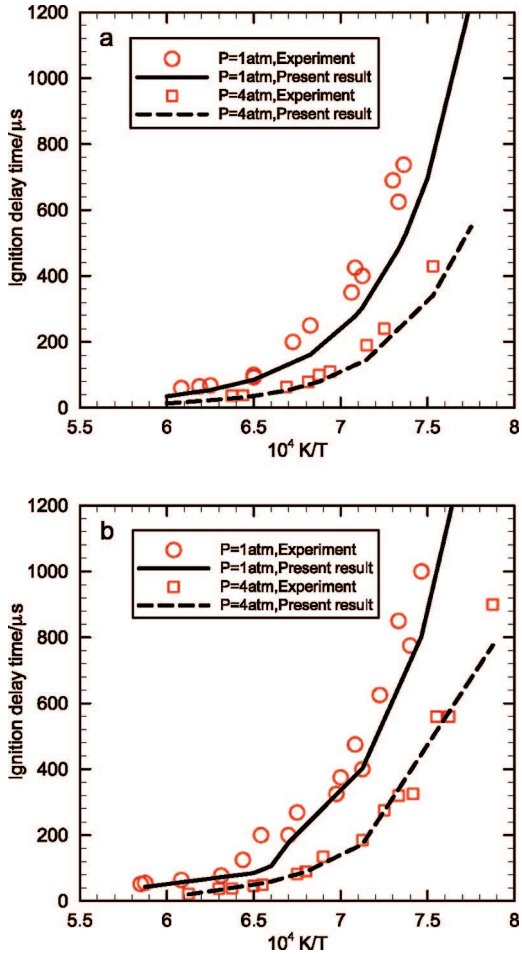


Figure 12. Calculated and measured ignition delay times of MB/O_2/Ar mixtures versus temperature for pressures of 1 and 4 atm at (a) equivalence ratio $\phi = 1$ and (b) equivalence ratio $\phi = 1.5$. Experimental data were taken from ref 8.

the mechanism. This pathway requires the inclusion of the methyl acetate decomposition submodel suggested by Westbrook and co-workers[10] in the kinetic mechanism.

The final kinetic model and associated thermochemistry will be available for download from the Web site of Prof. Violi at http://www-personal.umich.edu/~avioli/mechs.html.

4.3. CO_2 Prediction in Shock Tube Simulation. The new MB mechanism is used to study the formation of CO_2 in a shock tube. The "Reflected Shock Reactor" module of the Chemkin 4.1 package[33] is used to simulate the experiments. Shock tube simulations are zero-dimensional and begin at the onset of the reflected shock period assuming constant volume and homogeneous adiabatic conditions behind the reflected shock wave.

The experimental data have been recently obtained by the research group of Prof. Hanson at Stanford.[11] The reactor is fed with 2% MB in Ar, and two conditions were analyzed: (i) $T = 1260$ K and $P = 1.702$ atm and (ii) $T = 1426$ K and $P = 1.578$ atm. The comparison between the experimental data and the computed results for the concentration of CO_2 is reported in Figure 8.

The newly assembled kinetic model gives a very good agreement with the experimental CO_2 profiles for the two cases. The error is within 10% of the experimental data for the whole residence time. The concentration of CO_2 is controlled by both reactions R1 and R2, where reaction R1 is mainly responsible for CO_2 formation while reaction R2 is the main competing reaction of consuming CH_3OCO radical. Using the new MB model, rate-of-production (ROP) and sensitivity analyses for CO_2 formation were performed at the reflected shock tube conditions of 1426 K and 1.58 atm. Table 4 lists the main reactions involved in the formation of CO_2 for the shock tube simulations.

The ROP for CO_2 at 1426 K and 1.58 atm is presented in Figure 9 for the residence time τ between 0 and 1 ms. The two dominant pathways for the formation of CO_2 are the breaking of the C—O bond, via the decomposition of CH_3OCO (reaction R1) and $CH_3CH_2CH_2COO$ (reaction R8). The two reactions contribute evenly to the formation of CO_2 for the first ~0.05 ms; after that the contribution of R1 becomes slightly predominant.

Figure 10 shows the seven largest sensitivity coefficients at 1426 K and 1.58 atm. The sensitivity analysis supports the ROP interpretation. The concentration of CO_2 is strongly influenced by the initial decomposition pathways of MB through reaction R3 leading to the formation of $CH_3CH_2CH_2COO$ (BAOJ) and then CO_2 via R8 and to a less extent by reaction R7, whose product, $CH_2CO_2CH_3$, decomposes to form two separate oxygen-carrying moieties leading to the formation of CO. This explains the negative sensitivity values for reaction R7. The CO_2 concentration is also relatively sensitive to two of the MB + H hydrogen abstraction reactions, R4 and R6. The product of reaction R4, $CH_3CHCH_2COOCH_3$ (MB3J), breaks into C_3H_6 and CH_3OCO, which can form CO_2 through reactions R5. $CH_2CH_2CH_2COOCH_3$ (MB4J), a product from reaction R6, eventually produces CO through the CH_2COOCH_3 formation by the β-scission reaction (not given in Table 4). This explains the sign of the sensitivity coefficients for these reactions. In other words, the increase of the rate constants for reaction R4 (positive values) and R6 (negative values) will increase and decrease the CO_2 concentration, respectively. CH_3OCO can decompose to form either CO_2 or CO by reactions R1 and R2, respectively.

To understand further the formation of CO_2 during the MB breakdown, flux analyses were carried out using the new kinetic mechanism. Figure 11 shows the flux analyses for CO_2 formation in the shock tube ($T = 1426$ K and $P = 1.578$ atm) at a residence time of 0.1 ms (Figure 11a) and 0.4 ms (Figure 11b). In both cases, CO_2 is produced by two main pathways involving β-scission reactions.

At $\tau = 0.1$ ms, 87.1% CH_3OCO (through reaction R1) and 100% BAOJ (through reaction R8) are responsible for 56.5% and 43.5% CO_2 formation, respectively.

As the simulation proceeds, the CH_3OCO channel becomes more important, accounting for 74.1% of CO_2 formation compared to 25.9% for the BAOJ channel at $\tau = 0.4$ ms. CH_3OCO can be formed from MB directly through the unimolecular decomposition reaction (reaction R9) or indirectly through the hydrogen abstraction reactions to create MB3J and MP3J (reactions R4 and R10, respectively) and the combination between hydrogen abstraction and hydrogen migration from MBMJ (reaction R12 and R13). Note that CH_3OCO can directly dissociate to both CO_2 and CO at the same time, thus reactions R1 and R2 are important in CO_2 formation as presented in the sensitivity analysis (cf. Figure 10). For convenience in discussion, the net flux ratio between the two channels from CH_3OCH to CO_2 and CO can be denoted as ($CH_3OCO \rightarrow CO_2$) and ($CH_3OCO \rightarrow CO$), respectively. The net flux is the product (sum) of the forward and reverse flux for each channel. As the time elapses, the CO_2 dissociation channel becomes more and more important; particularly, the ($CH_3OCO \rightarrow CO_2$)/($CH_3OCO \rightarrow CO$) ratio is 6.7 and 7.4 at $\tau = 0.1$ and $\tau = 0.4$ ms, respectively.

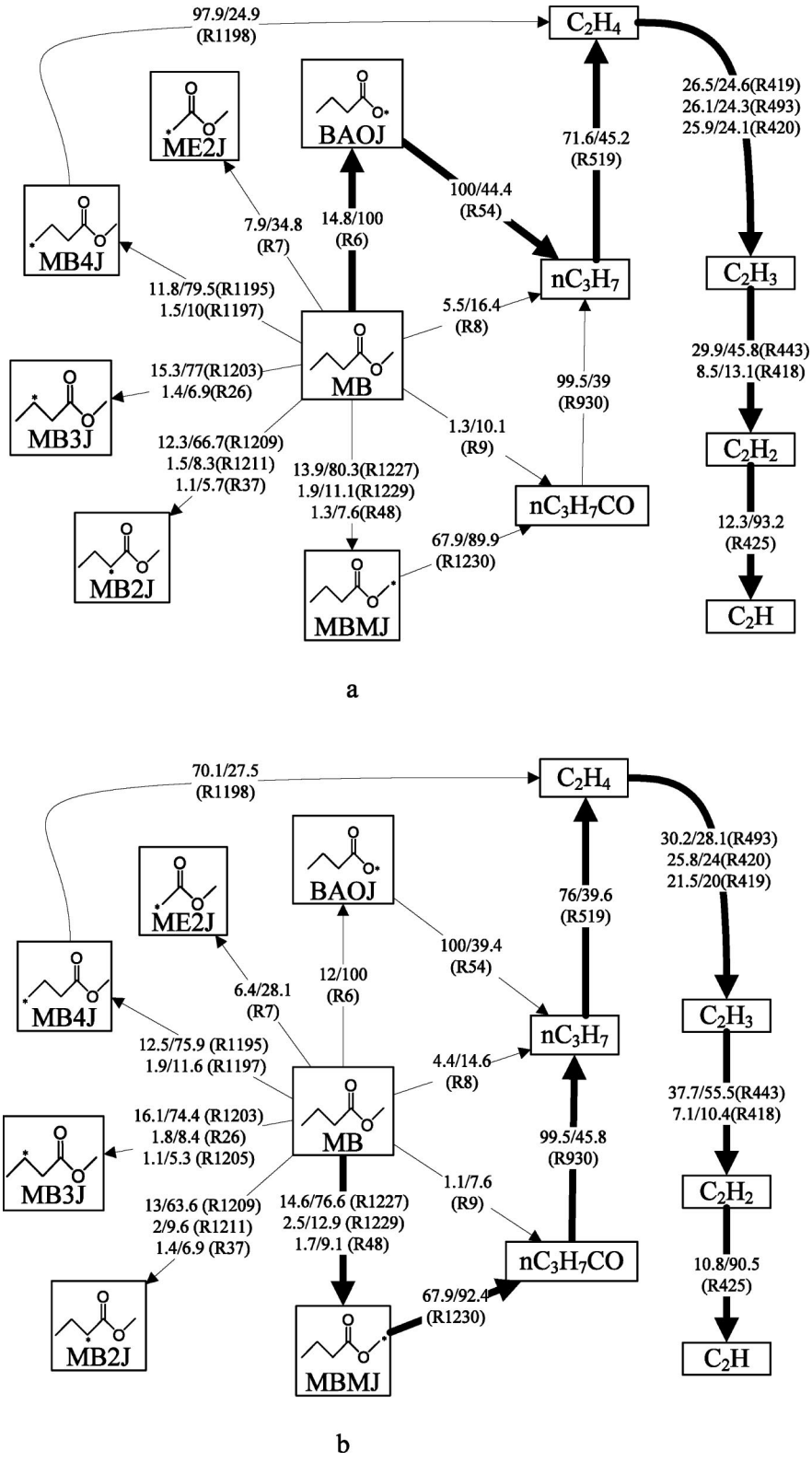


Figure 13. Flux analysis for the most important C_2H formation pathways and primary alkyl radical formation at $\phi = 1$ and two pressures: (a) 1 atm and (b) 4 atm. The notation "A/B" means A% reactant produces B% product in the considered channel; the reaction numbers are from the final MB kinetic mechanism.

The barrier height for the reaction $CH_3OCO = CH_3 + CO_2$ (R1) is lower than that of $CH_3OCO = CH_3O + CO$ (R2) by ~7.5 kcal/mol (cf. Table 3); thus in terms of chemical kinetics, rate constants of the latter reaction become comparable to those of the former at high temperatures. Note that in the shock tube reactor, the temperature decreases from the reflected shock temperature as the process proceeds due to the energy absorption in breaking chemical bonds. As temperature decreases reaction R1 to dominate over R2. This explains the increase trend of the $(CH_3OCO \rightarrow CO_2)/(CH_3OCO \rightarrow CO)$ ratio with the residence time.

4.4. MB Ignition Delay Times in Shock Tube. In order to provide more information on the combustion characteristics of MB and to extend the range of applicability of the new kinetic

mechanism, we carried out simulations of shock tube ignition delay times for MB. The experimental data were taken from Dooley et al.[8] The numerical simulations were performed using MB/O_2/Ar mixtures over the temperature range 1295−1632 K at reflected shock pressures of 1.0 and 4.0 atm and equivalence ratios of 1 and 1.5. We defined the ignition delay time as the time at which the maximum value of $[\dot{C}_2H] \times [\dot{O}]$ occurs.[35] Figure 12 presents the results of calculated ignition delay times of MB/O_2/Ar mixtures at different temperatures, pressures, and equivalence ratios, together with the experimental data from the literature.[8] The MB/O_2/Ar mixtures in the shock tube contain 1% MB, 13% O_2, and 86% Ar for an equivalence ratio of 1 and 1.5% MB, 6.5% O_2, and 92% Ar for an equivalence ratio of 1.5. The kinetic mechanism correctly reproduces the experimental data as function of the temperature, pressure, and equivalence ratios.

To analyze the important channels that determine the ignition delay times in different conditions, a detailed analysis of the rates of production for net and major reaction pathways for O and C_2H was carried out. Reactions $H + O_2 = OH + O$ and $C_2H_2 + OH = C_2H + H_2O$ are the dominant reactions for the formation of O and C_2H radicals, respectively.

Figure 13 shows the reaction pathways for the formation of C_2H and primary alkyl radicals at an equivalence ratio of 1 and pressures equal to 1 atm (Figure 13a) and 4 atm (Figure 13b).

The reaction pathways were extracted at 50% MB consumption. In Figure 13a, the pressure of 1 atm corresponds to a time of 8 μs and a temperature of 1475 K with a simulated ignition delay of 100 μs. The main pathways contributing to the formation of C_2H are

$$\mathrm{MB} \rightarrow \mathrm{BAOJ} \rightarrow n\text{-}C_3H_7 \rightarrow C_2H_4 \rightarrow C_2H_3 \rightarrow C_2H_2 \rightarrow C_2H$$

Produced from MB by C−O bond scission through reaction R-6, BAOJ undergoes β scission to form nC_3H_7 that further reacts to form ethane. Ethene subsequently decomposes via a series of hydrogen abstraction reactions to yield C_2H. The fuel radical formed in the largest quantity is MBMJ (17%), which also contributes to the formation of C_2H. The other two most abundant radicals are MB3J and MB2J. In Figure 13b, the pressure of 4 atm corresponds to a time of 6 μs and a temperature of 1480 K with a simulated ignition delay of 40 μs. As the pressure increases, the presence of MB3J among the fuel radicals becomes significant reaching 19%, followed by MBMJ with 18.8%, and MB2J with 16.4%. The main pathways of for the formation of C_2H are

$$\mathrm{MB} \rightarrow \mathrm{MBMJ} \rightarrow n\text{-}C_3H_7CO \rightarrow n\text{-}C_3H_7 \rightarrow C_2H_4 \rightarrow C_2H_3 \rightarrow C_2H_2 \rightarrow C_2H$$

MBMJ (18.8%) leads to the formation of ethene via a series of C–O and C−C bond breaking, and finally the C_2H radical is produced via hydrogen abstraction reactions.

5. Conclusions

This paper reports on new reaction pathways for the breakdown of methyl butanoate obtained using quantum mechanics and direct dynamics methods. The pathways and the reaction rates were computed using ab initio methods. This submechanism is coupled to the kinetic mechanism reported by Fisher et al. [*Proc. Combust. Inst.* **2000**, *28*, 1579] together with the addition of the six-centered unimolecular elimination reaction that yields ethylene and methyl acetate and the inclusion of the methyl acetate decomposition model. This new mechanism is then used to predict the mole fractions of CO_2 in shock tube experiments available in the literature. The capability of CO_2 prediction was improved by obtaining accurate rate constants for reactions $CH_3OCO = CH_3 + CO_2$ and $CH_3OCO = CH_3O + CO$ using the Rice−Ramsperger−Kassel−Marcus theory with corrections from tunneling, hindered rotation, and variational treatments.

The computed CO_2 concentration profiles are in very good agreement with the experimental data. Rate-of-production and sensitivity analyses are carried out for the new mechanism, and other kinetics available in the literature to investigate the pathways for the formation of CO_2 during the MB breakdown.

The MB mechanism was also used to simulate ignition delay times in the shock tube. Under the effect of temperature, pressure, and equivalence ratio, the results of simulation are consistent with experimental data. Reactions $H + O_2 = OH + O$ and $C_2H_2 + OH = C_2H + H_2O$ are found to be the dominant reactions for the formation of O and C_2H radicals, respectively. In addition, the pressure (in the correlation with temperature) affects the variation of predominant reaction pathways for the C_2H radical and primary alkyl radical formed from MB.

The new MB mechanism is able to correctly predict the concentration profiles of CO_2 in pyrolysis conditions as well as ignition delay time in oxidation conditions, thus giving a better chemical insight of combustion/pyrolysis of MB. Such results are encouraging, and this mechanism can be used as a basis for future implementations of the kinetics of biodisel esters.

Acknowledgment. This research is funded in part by the U.S. Air Force Scientific Office for Research (Grant FA9550-06-1-0376). The authors are grateful to Prof. R. Hanson for the data on shock tube experiments, to Dr. C. Westbrook for providing the kinetic mechanism for alkyl esters, and to Dr. H.-H. Carstensen for discussion on calculation of thermodynamic properties.

References and Notes

(1) Graboski, M. S.; McCormick, R. L. *Prog. Energy Combust. Sci.* **1998**, *24*, 125.
(2) Hill, J.; Nelson, E.; Tilman, D.; Polasky, S.; Tiffany, D. *Proc. Natl. Acad. Sci. U.S.A.* **2006**, *103*, 11206.
(3) Fisher, E. M.; Pitz, W. J.; Curran, H. J.; Westbrook, C. K. *Proc. Combust. Inst.* **2000**, *28*, 1579.
(4) Gail, S.; Thomson, M. J.; Sarathy, S. M.; Syed, S. A.; P. Dagaut b; Dievart, P.; Marchese, A. J.; Dryer, F. L. *Proc. Combust. Inst.* **2007**, *31*, 305.
(5) Metcalfe, W. K.; Dooley, S.; Curran, H. J.; Simmie, J. M.; Al-Nahas, A. M.; Navarro, M. V. *J. Phys. Chem. A* **2007**, *111*, 4001.
(6) Huynh, L. K.; Violi, A. *J. Org. Chem.* **2008**, *73*, 94.
(7) Westbrook, C. K.; Pitz, W. J.; Curran, H. J. *J. Phys. Chem. A* **2006**, *110*, 6912.
(8) Dooley, S.; Curran, H. J.; Simmie, J. M. *Combust. Flame* **2008**, *153*, 2.
(9) El-Nahas, A. M.; Navarro, M. V.; Simmie, J. M.; Joseph, W.; Bozzelli; Curran, H. J.; Dooley, S.; Metcalfe, W. *J. Phys. Chem. A* **2007**, *111*, 3727.
(10) Westbrook, C. K.; Pitz, W. J.; Westmoreland, P. R.; Dryer, F. L.; Chaos, M.; Osswald, P.; Kohse-Hoinghaus, K.; Cool, T. A.; Wang, J.; Yang, B.; Hansen, N.; Kasper, T. *Proc. Combust. Inst.* Accepted.
(11) Farooq, A.; Davidson, D. F.; Hanson, R. K.; Huynh, L. K.; Violi, A. *Proc. Combust. Inst.* Accepted.
(12) McCunn, L. R.; Lau, K.-C.; Krisch, M. J.; Butler, L. J.; Tsung, J.-W.; Lin, J. J. *J. Phys. Chem. A* **2006**, *110*, 1625.
(13) Glaude, P. A.; Pitz, W. J.; Thomson, M. J. *Proc. Combust. Inst.* **2005**, *30*, 1111.
(14) Frisch, M. J.; Trucks, G. W.; Schlegel, H. B.; Scuseria, G. E.; Robb, M. A.; Cheeseman, J. R.; Montgomery, J. A., Jr.; Vreven, T.; Kudin, K. N.; Burant, J. C.; Millam, J. M.; Iyengar, S. S.; Tomasi, J.; Barone, V.; Mennucci, B.; Cossi, M.; Scalmani, G.; Rega, N.; Petersson, G. A.; Nakatsuji, H.; Hada, M.; Ehara, M.; Toyota, K.; Fukuda, R.; Hasegawa, J.; Ishida, M.; Nakajima, T.; Honda, Y.; Kitao, O.; Nakai, H.; Klene, M.; Li, X.; Knox, J. E.; Hratchian, H. P.; Cross, J. B.; Adamo, C.; Jaramillo, J.; Gomperts, R.; Stratmann, R. E.; Yazyev, O.; Austin, A. J.; Cammi, R.;

Pomelli, C.; Ochterski, J. W.; Ayala, P. Y.; Morokuma, K.; Voth, G. A.; Salvador, P.; Dannenberg, J. J.; Zakrzewski, V. G.; Dapprich, S.; Daniels, A. D.; Strain, M. C.; Farkas, O.; Malick, D. K.; Rabuck, A. D.; Raghavachari, K.; Foresman, J. B.; Ortiz, J. V.; Cui, Q.; Baboul, A. G.; Clifford, S.; Cioslowski, J.; Stefanov, B. B.; Liu, G.; Liashenko, A.; Piskorz, P.; Komaromi, I. ; Martin, R. L.; Fox, D. J.; Keith, T.; Al-Laham, M. A.; Peng, C. Y.; Nanayakkara, A.; Challacombe, M.; Gill, P. M. W.; Johnson, B.; Chen, W.; Wong, M. W.; Gonzalez, C.; Pople, J. A. GAUSSIAN03. In *Gaussian 03, Revision A.1*; Gaussian, Inc.: Pittsburgh, PA , 2003.

(15) Baboul, A. G.; Curtiss, L. A.; Redfern, P. C.; Raghavachari, K. *J. Chem. Phys.* **1999**, *110*, 7650.

(16) Gonzalez, C.; Schlegel, H. B. *J. Phys. Chem.* **1990**, *94*, 5523.

(17) Duncan, W. T.; Bell, R. L.; Truong, T. N. *J. Comput. Chem.* **1998**, *19*, 1039.

(18) Truong, T. N.; Nayak, M.; Huynh, H. H.; Cook, T.; Mahajan, P.; Tran, L.-T. T.; Bharath, J.; Jain, S.; Pham, H. B.; Boonyasiriwat, C.; Nguyen, N.; ersen, E.; Kim, Y.; Choe, S.; Choi, J.; Cheatham, T. E., III.; Facelli, J. C. *J. Chem. Inf. Model.* **2006**, *46*, 971.

(19) Forst, W. *Theory of Unimolecular Reactions*; Academic Press: New York, 1973.

(20) Gilbert, R. G.; Smith, S. C. *Theory of Unimolecular and Recombination Reactions*; Blackwell: Oxford, 1990.

(21) Zhang, S.; Truong, T. N. *J. Phys. Chem. A* **2001**, *105*, 2427.

(22) Miller, W. H. *J. Am. Chem. Soc.* **1979**, *101*, 6810.

(23) Truhlar, D. G.; Garrett, B. C. *Acc. Chem. Res.* **1980**, *13*, 440.

(24) Truhlar, D. G.; Isaacson, A. D.; Garrett, B. C. *Theory of Chemical Reaction Dynamics*; Baer, M., Ed.; CRC Press: Boca Raton, FL, 1985; Vol. 4; p 65.

(25) Truong, T. N.; Truhlar, D. G. *J. Chem. Phys.* **1990**, *93*, 1761.

(26) Ayala, P. Y.; Schlegel, H. B. *J. Chem. Phys.* **1998**, *108*, 2314.

(27) Pitzer, K. S.; Gwinn, W. D. *J. Chem. Phys.* **1942**, *10*, 428.

(28) Li, J. C. M.; Pitzer, K. S. *J. Phys. Chem.* **1956**, *60*, 466.

(29) Good, D. A.; Francisco, J. S. *J. Phys. Chem. A* **2000**, *104*, 1171.

(30) Montgomery, J. A., Jr.; Frisch, M. J.; Ochterski, J. W. *J. Chem. Phys.* **2000**, *112*, 6532.

(31) Truhlar, D. G.; Isaacson, A. D.; Garrett, B. C. Generalized Transition State Theory. In *Theory of Chemical Reaction Dynamics*; Baer, M., Ed.; CRC Press: Boca Raton, FL, 1985; Vol. 4; pp 65.

(32) Truhlar, D. G. Direct Dynamics Method for the Calculation of Reaction Rates In *The Reaction Path in Chemistry: Current Approaches and Perspectives*; Heidrich, D., Ed.; Kluwer Academic: Dordrecht, 1995; pp 229.

(33) Kee, R. J.; Rupley, F. M.; Miller, J. A.; Coltrin, M. E.; Grcar, J. F.; Meeks, E.; Moffat, H. K.; Lutz, A. E.; Dixon-Lewis, G.; Smooke, M. D.; Warnatz, J.; Evans, G. H.; Larson, R. S.; Mitchell, R. E.; Petzold, L. R., Reynolds, W. C.; Caracotsios, M.; Stewart, W. E.; Glarborg, P.; Wang, C.; McLellan, C. L.; Adigun, O.; Houf, W. G.; Chou, C. P.; Miller, S. F.; Ho, P.; Young, P. D.; Young, D. J.; Hodgson, D. W.; Petrova, M. V.; Puduppakkam, K. V. *CHEMKIN Release 4.1*; Reaction Design: San Diego, CA, 2006.

(34) Dagaut, P. *Phys. Chem. Chem. Phys.* **2002**, *4*, 1846.

(35) Grebe, J.; Homann, K. H. *Ber. Bunsen-Ges. Phys. Chem.* **1982**, *86*, 597.

JP804358R